RESEARCH ARTICLE
doi: 10.2306/scienceasia1513-1874.2026.076

ScienceAsia 52 (4): 2026: ID 2026076: **1–11**

A pH-sensitive nanoparticle delivering *Lonicera edulis* anthocyanins for combined anti-hepatoma and immunomodulatory therapy

Siqi Liu†, Shan Li†, Bohan Zhang, Yanlong Zhang, Xiangqian Jia*, Dandan Zhao*

Engineering Research Center of Agricultural Microbiology Technology, Ministry of Education & Heilongjiang Provincial Key Laboratory of Ecological Restoration and Resource Utilization for Cold Region & Key Laboratory of Microbiology, College of Heilongjiang Province & School of Life Sciences, Heilongjiang University, Harbin 150080 China

*Corresponding authors, e-mail: 2021108@hlju.edu.cn, 2004090@hlju.edu.cn
† These authors contributed equally to this work.

Received 15 Apr 2026, Accepted 20 Jul 2026
Available online 2 Sep 2026

ABSTRACT: Blue honeysuckle (*Lonicera edulis* L.) represents an emerging source of berries with significant biological activity. Nevertheless, the practical application of its anthocyanins in the food and medical sectors is constrained by their limited stability. This study focuses on anthocyanins extracted and purified from the pomace of *L. edulis* harvested in the Boli region of Heilongjiang Province, China. These anthocyanins served as the core material, while carboxymethyl chitosan (CMCS), L-histidine (L-His), and stearic acid (SA) were employed as carrier materials. A pH-sensitive micellar system, designated as CMCS-His-SA nanoparticles (NPs), was developed using the film dispersion technique and optimization of the preparation conditions. This pH-triggered size expansion (111.8 nm→570.9 nm, pH 7.4→6.5) enables selective drug release within acidic tumors. This study investigates the structural properties of CMCS-His-SA NPs at the material level. At the cellular level, HepG2 cells and RAW264.7 macrophages were utilized as model systems to evaluate the anti-hepatocarcinoma and immunomodulatory activities.

KEYWORDS: *Lonicera edulis*, anthocyanins, nanoparticle, HepG2 cells

INTRODUCTION

Blue honeysuckle (*Lonicera edulis* L.) is a member of Caprifoliaceae, genus *Lonicera*, subgenus *Lonicera*. It is mainly distributed in China, Russia, and Japan [1]. Blue honeysuckle has extremely strong cold and frost resistance and resistance to pests and diseases. It can survive even in low-temperature environments of −40 °C and bloom at −8 °C, making it known as "the emerging king of third-generation small berries [2]". Blue honeysuckle is a highly valuable berry for food and medicinal purposes due to its rich content of anthocyanins, polyphenols, and flavonoids [3, 4].

Anthocyanins are a water-soluble pigment and one of the main active ingredients in blue honeysuckle. Studies have shown that anthocyanins have strong anti-tumor activity [5] and can enhance serum antioxidant capacity to inhibit the oxidation of low-density lipoprotein and protect the cardiovascular system. Anthocyanins also have the functions of treating diabetes, preventing aging, and treating gastrointestinal diseases by controlling intestinal flora [6]. However, anthocyanins are readily affected by factors such as temperature, light, oxidants, reducing agents, metal ions, and pH [7], which limits their application in fields such as food and healthcare.

Nowadays, the threat of tumors to human health is increasing daily [8]. Tumors are among the leading causes of cancer-related mortality [9]. Commonly used anticancer drugs, such as doxorubicin [10], paclitaxel [11], and cisplatin [12], have problems including poor targeting, low stability, poor bioavailability, and significant side effects, which make it difficult to increase the cure rates of tumors. Nano-delivery systems, such as nanoparticles [13], liposomes [14], and nano-capsules, can address these limitations. Nanomedicines leverage the enhanced permeability and retention (EPR) effect [15]—the preferential accumulation of nanoparticles in tumors due to high vascular permeability and impaired lymphatic drainage—to passively target tumor sites, thereby increasing therapeutic efficacy. Among them, nanoparticles have attracted much attention due to their modifiability and material diversity. Therefore, this study adopted the method of nanoparticle-loaded anthocyanins to construct pH sensitive anti-tumor drugs and evaluate their activation of immune cells and anti-tumor activity.

The aim of this project is to improve the stability of anthocyanins and achieve the combination of tumor chemotherapy and immunotherapy by preparing blue honeysuckle anthocyanin nanoparticles (CMCS-His-SA NPs) and utilizing the advantages of pH responsiveness and targeting of the intelligent chitosan nano drug delivery system. Fig. 1 illustrates the mechanism by which the CMCS-His-SA nanocarrier delivers anthocyanins. As a by-product of industrial production, blue honeysuckle residue still contains a large number of anthocyanins. Through the research and utilization of anthocyanins in blue honeysuckle residue, it can turn waste into treasure, laying a theoretical foundation for

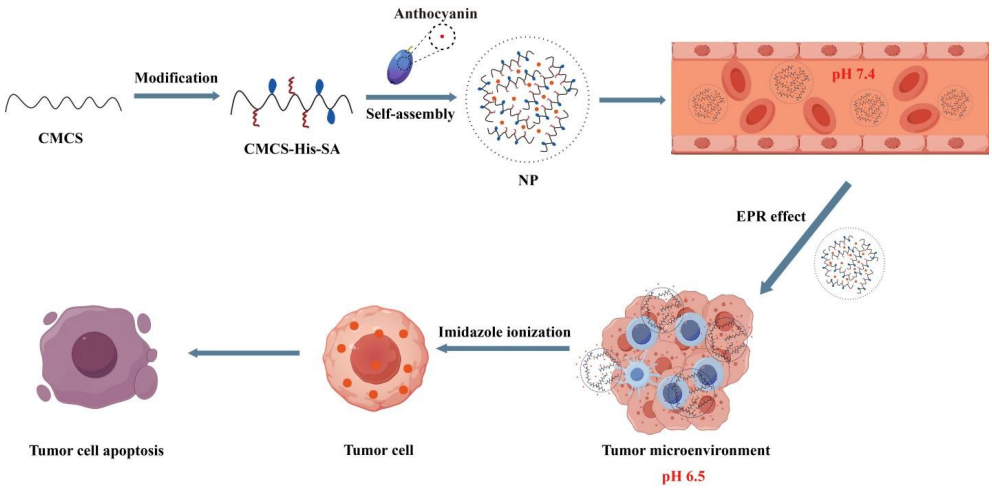

Fig. 1 Schematic illustration of the self-assembly of CMCS-His-SA NPs and the pH-responsive delivery of blue honeysuckle anthocyanins.

the application of blue honeysuckle anthocyanins in food and medicine.

MATERIALS AND METHODS

Materials

The blue honeysuckle residue is provided by Lijian Biotechnology Co., Ltd. in Boli County, Heilongjiang Province, China, and stored at −20 °C for future use. HepG2 cell (a human hepatocellular carcinoma cell line used as a standard model for liver toxicity, drug metabolism, and hepatocellular carcinoma research) and RAW264.7 cell (a mouse monocyte/-macrophage cell line commonly employed to study inflammation, immune response, and macrophage polarization mechanisms) were purchased from the Cell Bank of the Chinese Academy of Sciences in Shanghai. Carboxymethyl chitosan (molecular weight 240 kDa, degree of deacetylation >90%, degree of substitution 90%), N-hydroxysuccinimide, N,N′-dicyclohexylcarbodiimide, 4-dimethylaminopyridine, carbodiimide hydrochloride, stearic acid, and L-histidine were purchased from McLean Biochemical Technology Co., Ltd. (Shanghai, China). Fetal bovine serum, penicillin, streptomycin, Cell Counting Kit-8, and Hoechst 33258 staining solution were purchased from Biyun Tian Biotechnology Research Institute (Beijing, China). Premix Taq®, 1st Strand cDNA Synthesis Kit, SYBR® Premix Ex Taq™ (Takara Biotechnology (Dalian) Co., Ltd. (Dalian, China)), along with anhydrous ethanol, TRIzol® Reagent, PCR primers, polyamide, RPMI 1640 medium (Kaiji Biotechnology Co., Ltd., Jiangsu, China), were used in this study.

Extraction and purification of anthocyanins from blue honeysuckle

The blue honeysuckle residue was stored in a −20 °C freezer. The residue was crushed using a juicer and extracted the crushed residue with 85% ethanol solution (pH = 3) at a solid-to-solvent ratio of 1:10 using ultrasonic treatment for 40 min. The extraction was repeated three times under identical conditions. The filtrates were combined, concentrated by rotary evaporation, and then dried by vacuum freeze-drying to obtain the crude anthocyanin extract. Further purification of anthocyanins was performed using the method described by Xue et al [16].

Anthocyanin content was determined using the pH differential method [17]. Briefly, 1 ml aliquots of the diluted anthocyanin solution were prepared in two separate test tubes. Buffer solutions at pH 1.0 and pH 4.5 were added to each tube, mixed thoroughly, wrapped in aluminum foil, and incubated in darkness for 20 min. The A_{510} and A_{700} values for each solution were measured [18]. Anthocyanin content was calculated using the following equation:

$$\text{Extract quantity (mg/100g)} = \frac{A \times M_W \times \text{DF} \times \text{V}}{\epsilon \times L \times m} \times 100 \quad (1)$$

where $A = (A_{510} - A_{700})_{\text{pH 1.0}} - (A_{510} - A_{700})_{\text{pH 4.5}}$; M_W is the molecular weight of cyanidin-3-glucoside (449.2 g/mol); V is the volume of solution (ml); DF is the dilution factor; ε is the molar extinction coefficient of cyanidin-3-glucoside (26,900 l/mol/cm); L is the optical path (1 cm); and m is the mass of the dry fruit.

Purified anthocyanin powder was dissolved to prepare an anthocyanin solution, which was scanned using a UV–Visible spectrophotometer over the wavelength range of 200–800 nm to obtain the characteristic absorption peaks of blue honeysuckle anthocyanins.

Preparation of anthocyanin-loaded nanoparticles

Carboxymethyl chitosan (CMCS, 1 mol) was weighed and dissolved in 75 ml of ultrapure water. After complete dissolution, 1 mol of N-hydroxysuccinimide and

1.4 mol of carbodiimide hydrochloride were added. The mixture was stirred using a magnetic stirrer for 1 h, and then 0.5 mol of the weighed L-His was added. The mixture was then stirred at room temperature for 24 h. After stirring, the sample was transferred to a dialysis bag (with a molecular weight cut-off >3,500 Da), dialyzed against ultrapure water for 24 h, and vacuum-dried the product to obtain CMCS-His. Two hundred milligrams of the prepared CMCS-His powder was weighed and mixed thoroughly with 40 ml of dimethyl sulfoxide (DMSO) to obtain solution A. Eight millimoles of stearic acid (SA) was weighed and mixed with 40 ml of DMSO, 8 mmol of N,N′-dicyclohexylcarbodiimide, and 9.6 mmol of 4-dimethylaminopyridine, and the mixture was stirred at room temperature for 2 h to obtain solution B. Solutions A and B were mixed and stirred at 75 °C for 4 h, after which the mixture was transferred to a dialysis bag (with a molecular weight cut-off >3,500 Da) at room temperature and dialyzed against deionized water for 24 h to remove DMSO. The dialyzed sample was transferred into a separatory funnel, an equal volume of ethyl acetate was added for extraction, the extraction was repeated three times to remove excess components, the sample was evaporated at 40 °C, and then the product was vacuum-dried to obtain CMCS-His-SA [19]. Following the method described by Sulaiman and Rajab [20], anthocyanin-loaded nanoparticles were prepared using the film-dispersion method.

Characterization of CMCS-His-SA and CMCS-His-SA NPs

Five milligrams of CMCS-His-SA, CMCS-His, CMCS, His and SA were weighed; the samples were prepared using the KBr compression method. The samples were then analyzed by Fourier transform infrared (FTIR) spectroscopy over the range of 4000–400 cm^{-1} to obtain their infrared spectra. Five milligrams of the CMCS-His-SA sample were weighed and dissolved in 0.5 ml of deuterated DMSO. The solution was mixed thoroughly and transferred into an NMR tube for ^{1}H-NMR analysis at 25 °C. CMCS-His-SA blank NPs with pH 7.4 and pH 5.0 were prepared by the thin-film dispersion method, and their particle size was measured at different pH values using a dynamic light scattering instrument, and the particle size distribution curve was plotted. CMCS-His-SA NPs with pH 7.4, pH 6.5 and pH 5.0 were prepared using the thin-film dispersion method, and their zeta potential was analyzed at different pH values. CMCS-His-SA blank nanoparticles at concentrations of 10, 20, 30, 40, 50, 80, 110, 140, 170, and 200 µg/ml were prepared using the thin-film dispersion method. The conductivity was measured at different concentrations at room temperature, and the critical micelle concentration of CMCS-His-SA blank nanoparticles was determined by taking the turning point in the graph. Following the method described by Aldawsari et al [21], the particle size and zeta potential of the nanoparticles were measured, and transmission electron microscopy (TEM) observations were performed.

Cytotoxicity of CMCS-His-SA NPs and morphological evaluation of HepG2 cells

CMCS-His-SA blank nanoparticles were prepared using the thin-film dispersion method. Human kidney-derived cells 293T were cultured and passaged for detecting cytotoxicity. After cell counting, the cells were seeded into a 96-well plate at a density of 1×10^4 cells/well. The cells were cultured in a cell culture incubator (37 °C, 5% CO_2) for 24 h, and then the medium was aspirated. Ten microliters of CMCS-His-SA blank nanoparticle solution at concentrations of 25, 50, 100, 200, 400, and 800 µg/ml were added to each well. The blank group was treated with 100 µl of DMEM medium (containing 10% fetal bovine serum and 1% penicillin streptomycin), with three replicates set for each concentration. After 24 h of drug application, 10 µl of DMEM medium (containing 10% fetal bovine serum and 1% penicillin streptomycin) was added to each well. After 30 min, the OD_{450} value was measured using a microplate reader. The cell survival rate was calculated using the following equation:

$$\text{Cell survival rate (\%)} = \frac{OD_{sample} - OD_{blank}}{OD_{control} - OD_{blank}} \times 100\% \quad (2)$$

OD_{sample}: the OD_{450} values of experimental wells containing CMCS-His-SA NPs at different concentrations; $OD_{control}$: the OD_{450} value of normal cell pores containing only cells (no NPs or drugs); OD_{blank}: the OD_{450} value for wells containing only DMEM medium (cell-free), used to correct for the background absorbance of the medium.

Cytotoxicity and behavioral evaluation of CMCS-His-SA NPs on RAW264.7 cells

CMCS-His-SA blank nanoparticles were prepared using the thin-film dispersion method. RAW264.7 macrophages were revived and cultured for passage. After cell counting, the cells were seeded into a 96-well plate at a density of 1×10^4 cells/well. After 24 h of cultivation in a cell culture incubator (37 °C, 5% CO_2), the medium was aspirated, and 10 µl of CMCS His SA blank nanoparticles solution at concentrations of 50, 100, 200, 400, and 800 µg/ml were added to each well. The blank group was treated with only 100 µl of DMEM medium (containing 10% fetal bovine serum and 1% penicillin streptomycin), with three replicates set for each concentration. After 24 h of drug application, 10 µl of CCK-8 was added to each well. After adding the Cell Counting Kit-8 reagent and incubating for 30 min, the OD_{450} value was measured using a microplate reader, and the cell survival rate was calculated according to Eq. (2). Behavioral evaluation was also conducted on RAW264.7 cells [22].

Statistical analysis

All experiments were repeated three times, and the experimental data were expressed as mean ± standard deviation (SD) using a non-paired two-tailed t-test. Compared with the control group, ns, $p > 0.05$, no statistical significance, $^{*}\,p < 0.05$ indicates significant difference, and $^{**}\,p < 0.01$ indicates extremely significant difference, with statistical significance.

RESULTS AND DISCUSSION

Extraction and purification of anthocyanins from blue honeysuckle pomace

Anthocyanins were extracted under the following conditions: a solid-to-liquid ratio of 1:10, an ethanol concentration of 85%, and 40 min of extraction using a 100 W immersion ultrasonicator. According to Eq. (1), the anthocyanin content was determined to be 0.942 g per 100 g of blue honeysuckle, which is equivalent to approximately 0.942 g of crude anthocyanin extract per 100 g of blue honeysuckle pomace. After purification using polyamide resin, the anthocyanin purity increased to 4.702 g per 100 g of the crude extract.

For sample loading using anthocyanin solution, samples were collected every 5 min and absorbance was measured at 520 nm using a UV-Vis spectrophotometer. A breakthrough curve was plotted as shown in Fig. 2(A). With increasing sample loading volume, the absorbance gradually increased. When the number of collected fractions reached 113, the absorbance of the effluent was one-tenth of that of the loading solution. However, the required number of collection tubes may vary depending on the collection volume and is not fixed. At this point, the cumulative loading volume was 565 ml, indicating that breakthrough had occurred; therefore, loading was stopped. From the dynamic elution curve in Fig. 2(B), the A_{520} first increased and then decreased with increasing sample volume. When 104 fractions had been collected, corresponding to a sample volume of 520 ml, the A value reached its maximum. When 178 fractions had been collected, corresponding to a sample volume of 890 ml, no anthocyanins were detected. Fig. 2(C) shows the standard curve for anthocyanins, and the regression equation is $Y = 0.001494X + 0.05313$, with an R^2 value of 0.9991.

The extracted anthocyanins were analyzed using UV-Visible spectroscopy. As shown in Fig. 2(D), anthocyanins have two characteristic absorption peaks around 500–540 nm and 275 nm, respectively. Therefore, we can confirm that they are anthocyanins [23].

Synthesis, preparation, and characterization of CMCS-His-SA conjugate

Nanoparticles are a type of self-assembling nanocarrier, which is a promising biomaterial with a wide range of applications. Jiang et al [24] designed a pH- and hypoxia-responsive γ-Fe_2O_3/isosorbide nitrate carrier micelle based on carboxymethyl chitosan, which catalyzes endogenous H_2O_2 to produce oxygen and alleviate TME hypoxia, thereby reducing the overexpression of HIF-1α and PD-L1 in tumors. Meanwhile, it reacts with H_2O_2 to release ROS via the Fenton reaction, inducing cytotoxicity in tumor cells [24]. Mubeen et al [25] prepared paclitaxel-loaded linoleic acid carboxymethyl chitosan nanoparticles for oral administration of paclitaxel, which plays a crucial role in enhancing oral bioavailability and solubility. This experiment utilized carboxymethyl chitosan to prepare nanoparticles, thereby expanding its potential applications.

Infrared spectral analysis

Fig. 3(A) shows the infrared spectra of CMCS, His, SA, CMCS-His, and CMCS-His-SA. In the FTIR spectrum of CMCS-His, stretching vibrations were identified at 1638 and 1560 cm^{-1}, corresponding to the C=N and N—H groups of the His moiety, respectively. In the spectrum of CMCS-His-SA, a significant change can be observed at 2920 cm^{-1}, indicating the presence of $-CH_3$ and $-CH_2$, as well as a change at 1704 cm^{-1}, indicating the C=O group in the ester bond [26]. This demonstrates the successful integration of stearic acid into the structural backbone of CMCS during the reaction process.

Nuclear magnetic resonance analysis of CMCS-His-SA

Fig. 3(B) shows the ^{1}H NMR spectrum of CMCS-His-SA. As shown in Fig. 3(B), the new peak at 6.74 ppm is assigned to the proton of the imidazole group in the His moiety. The peak at 2.10–2.29 ppm is attributed to the methylene group next to the carbonyl group, whereas the peak at 1.51 ppm corresponds to the methylene group α to the carbonyl group. All other methylene groups show a peak at 0.84 ppm. The broadening peak of methylene (1.96 ppm) near the ester bond (1.37 ppm) indicates the successful esterification of CMCS-His with SA.

Particle size analysis of CMCS-His-SA blank Nanoparticles under different pH conditions

Fig. 3(C, D) shows the particle size analysis of CMCS-His-SA blank nanoparticles at pH 7.4 and pH 5.0. As shown in Fig. 3(C), the particle size of CMCS-His-SA blank nanoparticles at pH 7.4 was 198.3 ± 21.9 nm, with a PDI of 0.248 ± 0.008. As shown in Fig. 3(D), the particle size of CMCS-His-SA blank nanoparticles under acidic conditions (pH 5.0) was 475.73 ± 22.28 nm, with a PDI of 0.302 ± 0.028. Previous studies have shown that the particle size of nanoparticles increases as pH decreases. When the pH drops to acidic values, the imidazole group of histidine becomes protonated, causing nanoparticle expansion due to repulsion, which results in increased particle size and pH

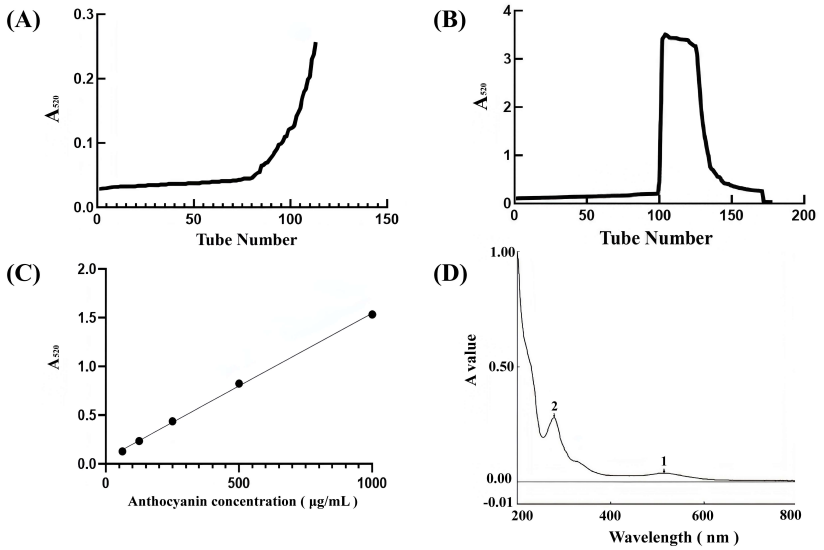

Fig. 2 (A) Breakthrough curve; (B) Dynamic elution curve; (C) Anthocyanin standard curve; (D) UV–Vis full-wavelength scanning image.

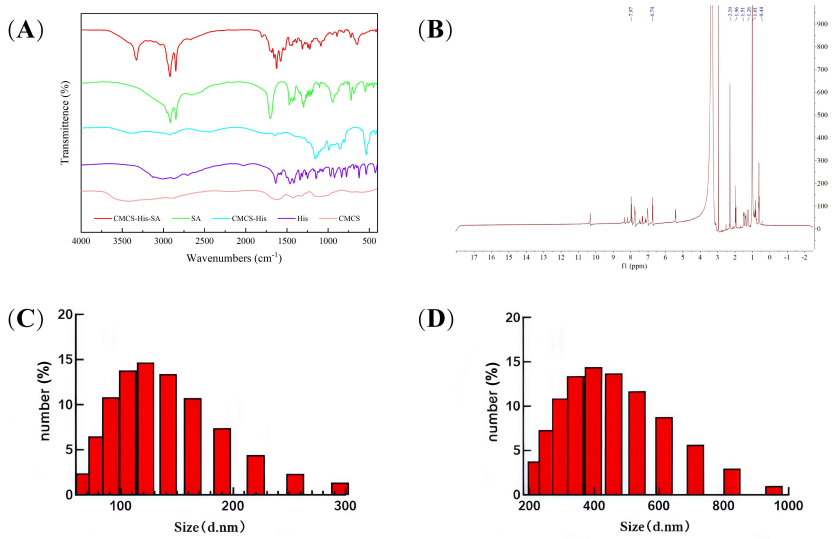

Fig. 3 (A) Infrared spectra of CMCS, His, SA, CMCS-His, and CMCS-His-SA; (B) ^{1}H NMR spectrum of CMCS-His-SA; (C, D) Particle size distribution map of CMCS-His-SA at pH 7.4 and 5.0 (d = diameter).

sensitivity. These results indicate successful preparation of pH-responsive nanoparticles.

Zeta potential analysis of CMCS-His-SA blank Nanoparticles under different pH conditions

Table 1 shows the zeta potential of CMCS-His-SA blank nanoparticles under different pH conditions. The zeta potential of CMCS-His-SA blank nanoparticles was -13.1 ± 0.45 mV at pH 7.4 and 4.7 ± 0.14 mV at pH 5.0, indicating that their charge reverses from negative to positive under acidic conditions. This is because the ionization of the histidine imidazole group causes a change in charge, and the nanoparticles also become unstable due to acidic changes in pH, gradually expanding and cracking. The combined effects of the above processes cause the nanoparticles to exhibit a characteristic behavior of "swelling → partial disintegration → drug release" in an acidic microenvironment. This design is specifically tailored to the acidic microenvironment of solid tumors (pH 5.0–6.5), demonstrating the advantages of the smart responsive design of the carrier system—remaining stable in a normal physiological environment while triggering the release mechanism upon reaching the tumor site [27–29].

Compared with traditional systems (liposomes [30] and PEG Nanoparticles [31]), CMCS-His-SA NPs offer the following key

Table 1 Zeta potential of CMCS-His-SA blank nanoparticles under different pH conditions.

pH of CMCS-His-SA blank nanoparticles	Zeta potential (mV)
7.4	−13.1 ± 0.45
5.0	4.7 ± 0.14

Table 2 Zeta potential of CMCS-His-SA NPs at different pH conditions.

pH of CMCS-His-SA NPs	Zeta potential (mV)
7.4	−15.9 ± 0.78
6.5	2.34 ± 0.19
5.0	6.34 ± 0.3

advantages: The preparation process utilizes polyelectrolyte self-assembly technology, eliminating complex emulsification and lyophilization steps, thereby reducing costs and enabling large-scale production; Tumor targeting utilizes pH-induced charge reversal—maintaining a negative charge (−13.1 ± 0.45 mV) at pH 7.4 to minimize clearance by the reticuloendothelial system during circulation, followed by a switch to a positive charge (4.7 ± 0.14 mV) at pH 5.0 to actively enhance cell membrane adsorption and endocytosis at the tumor site; and cost-effectiveness stems from the use of stable and inexpensive carboxymethyl chitosan as the raw material. In summary, this system outperforms conventional delivery systems in terms of process simplicity, targeting specificity, circulatory stability, and cost-effectiveness, demonstrating significant clinical potential [32, 33].

Analysis of critical micelle concentration (CMC) of CMCS-His-SA blank nanoparticles

Fig. 4(A) shows the determination of CMC of CMCS-His-SA blank nanoparticles by the conductivity method. The CMC is the lowest concentration at which surfactant molecules coalesce to form nanoparticles and is an important parameter for determining the thermodynamic stability of micelle delivery systems [34]. The results in Fig. 4(A) indicate that the CMC of CMCS-His-SA blank nanoparticles is 69.62 µg/ml, which is significantly lower than that of other surfactants, suggesting that the nanoparticles can be readily formed.

Characterization of CMCS-His-SA NPs

Fig. 4(B–D) shows the particle size analysis of CMCS-His-SA NPs at different pH values. Fig. 4(B) shows the particle size of CMCS-His-SA NPs at pH 7.4, which was 111.83 ± 1.3 nm, with a PDI of 0.163 ± 0.024. Fig. 4(C) shows the particle size of CMCS-His-SA NPs at pH 6.5, which was 117.78 ± 7.14 nm, with a PDI of 0.27 ± 0.022. Fig. 4(D) shows the particle size of CMCS-His-SA NPs at pH 5.0, which was 570.9 ± 15.8 nm, with a PDI of 0.342 ± 0.028. The particle size increased by approximately 5-fold when pH decreased from 7.4 to 5.0, demonstrating that CMCS-His-SA NPs are pH-sensitive intelligent NPs. Under acidic conditions, the imidazole group of histidine becomes protonated, and the pKa of the imidazole group is approximately 6.5. Ionized monomers form strong electrostatic repulsion, causing the structure to gradually expand and the particle size to increase accordingly [35].

Table 2 shows the zeta potential of CMCS-His-SA NPs under different conditions. The results indicate that the zeta potential of CMCS-His-SA NPs changes with pH variation. The zeta potential of CMCS-His-SA NPs at pH 7.4 is around −15.9 mV. At pH 6.5, the zeta potential of CMCS-His-SA NPs reversed from negative to positive, reaching approximately 2.34 mV. At pH 5.0, the zeta potential of CMCS-His-SA NPs is around 6.34 mV. This is due to ionization of the imidazole group of histidine, causing a change in the zeta potential of CMCS-His-SA NPs from negative to positive. As the pH of CMCS-His-SA NPs decreases, they gradually expand and their particle size increases.

Fig. 4(E) shows the TEM image of CMCS-His-SA NPs. We observed that CMCS-His-SA NPs exhibited a uniform and stable spherical shape, with particle sizes consistent with those measured by dynamic light scattering (DLS). These results confirm the successful preparation of CMCS-His-SA NPs. In summary, a CMCS-His-SA NPs loaded with anthocyanins was prepared in this study. His was used as the pH-sensitive component, and SA was used as the hydrophobic end. The NPs were characterized by ^{1}H NMR spectroscopy, FTIR spectroscopy, TEM, particle size analysis, and zeta potential analysis. The particle size was 111.83 nm. Zeta potential showed that the charge reversed from negative to positive from pH 7.4 to pH 5.0, and the particle size increased, confirming the successful preparation of indigo fruit anthocyanin nanoparticles.

Anti-hepatocellular carcinoma activity of CMCS-His-SA NPs against HepG2 cells

Cytotoxicity of CMCS-His-SA blank nanoparticles toward human kidney-derived 293T cells

Fig. 5(A) shows the survival rate of human embryonic kidney (HEK293T) cells after treatment with CMCS-His-SA blank nanoparticles. Cytotoxicity testing is an important part of the safety evaluation of biopharmaceutical materials, and its results can indicate whether the biomaterials and their related components are biologically safe [36]. Cytotoxicity testing using the CCK-8 kit showed that the cell survival rate of human kidney-derived 293T cells remained above 90% after incubation with CMCS-His-SA blank nanoparticles at concentrations of 25–800 µg/ml for 24 h (Fig. 5(A)).

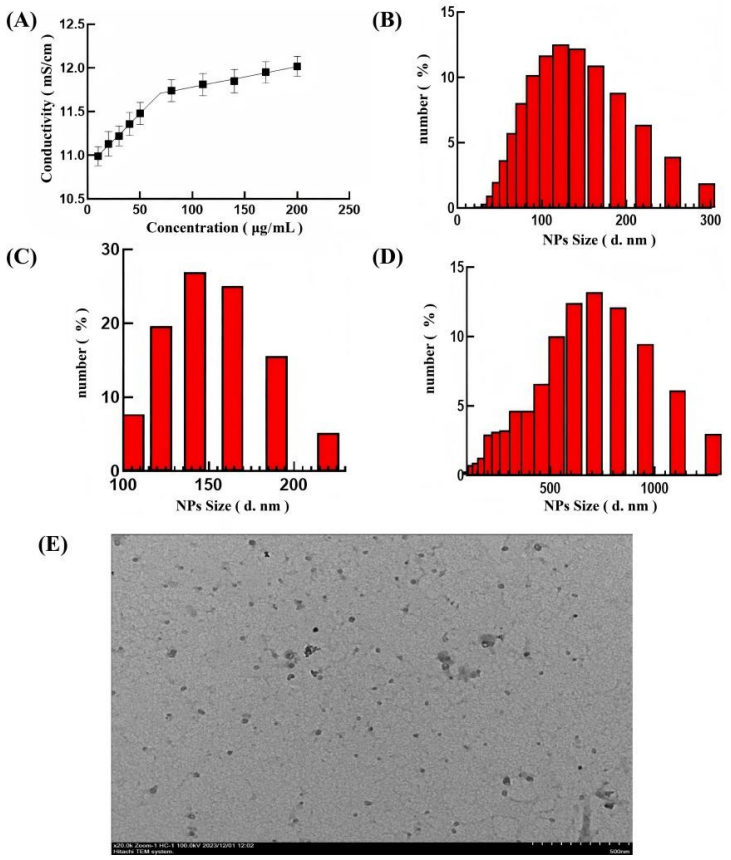

Fig. 4 (A) CMC of CMCS-His-SA blank nanoparticles; (B–D) Particle size distribution maps of CMCS-His-SA NPs (NPs = CMCS-His-SA NPs, d = diameter) at pH 7.4, 6.5, and 5.0, respectively; (E) TEM images of NPs.

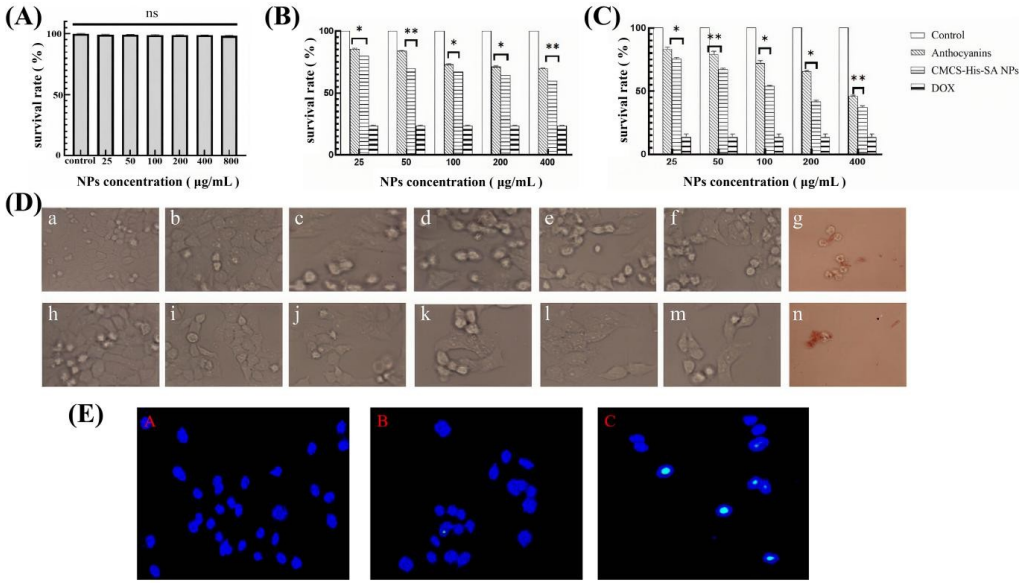

Fig. 5 (A) Cytotoxicity of CMCS-His-SA blank nanoparticles toward human kidney-derived 293T cells (NPs = CMCS-His-SA NPs). Proliferation of HepG2 cells treated with (B) anthocyanins and (C) NPs. (D) Inverted microscopy images of morphological changes in HepG2 cells treated with NPs (200×): (a) 24 h control group; (b) 24 h DOX group; (c–g): 25, 50, 100, 200, 400 μg/ml CMCS-His-SA NPs groups; (h) 48 h control group; (i–m): 25, 50, 100, 200, 400 μg/ml CMCS-His-SA NPs group; (n) 48 h DOX group. (E) Fluorescence images of nuclei in HepG2 hepatocellular carcinoma cells (100×): (a) 24 h control group; (b, c) 200 and 400 μg/ml NPs treatment groups after 24 h.

Although the cell survival rate showed a decreasing trend with increasing concentrations of CMCS-His-SA blank nanoparticles, there was no significant difference among the different concentrations. For subsequent experiments, drug loading concentrations of 25–400 μg/ml were selected. The cytotoxicity test showed that CMCS-His-SA conjugates have low cytotoxicity and can be used as carriers for tumor drug delivery. At the same time, CMCS, as the main component of CMCS-His-SA conjugates, is a natural polysaccharide. Compared with chitosan, it has better biocompatibility and biodegradability.

The effect of CMCS-His-SA NPs on the proliferation of HepG2 cells

Fig. 5(B, C) shows the effects of anthocyanins and CMCS-His-SA NPs on the proliferation of HepG2 cells after 24 h and 48 h of treatment, respectively. The results showed that both anthocyanins and CMCS-His-SA NPs could inhibit the proliferation of HepG2 cells. At 25 μg/ml, a significant inhibitory effect was observed, and the inhibitory effect on the proliferation of HepG2 cells also increased with increasing drug concentration and treatment time. At 400 μg/ml, the difference in the inhibitory effects of anthocyanins and CMCS-His-SA NPs on the proliferation of HepG2 cells was the greatest, at 10.13%. This may be because CMCS-His-SA NPs are acid-sensitive intelligent NPs that release drugs faster in the acidic environment of tumor cells.

In summary, the anti-hepatocellular carcinoma activity of CMCS-His-SA NPs is significantly better than that of indigo anthocyanins, and the difference in the inhibition rate against HepG2 cells between the two increases with increasing concentration and treatment time.

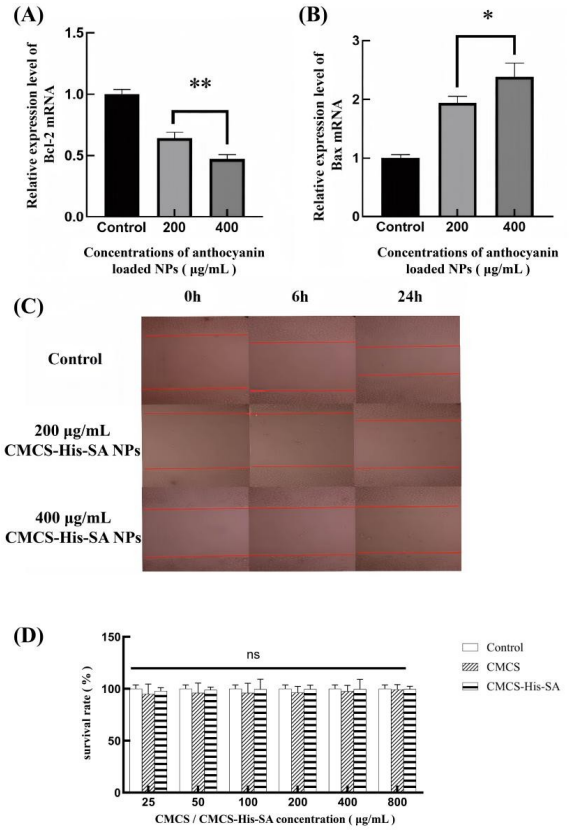

Fig. 6 (A) The effect of NPs (NPs = CMCS-His-SA NPs) on *Bcl-2* expression in HepG2 cells; (B) *Bax* expression in HepG2 cells; (C) HepG2 cell migration; (D) CMCS and CMCS-His-SA blank nanoparticles on the viability of RAW264.7 cells.

The effect of CMCS-His-SA NPs on apoptosis of HepG2 cells

After HepG2 cells were treated with CMCS-His-SA NPs for 24 h and 48 h, their morphology was observed under an inverted microscope (Fig. 5D). Fig. 5D(a, h) shows the blank control group at 24 h and 48 h, respectively. The cell density in the blank control group was high, and the cells were in good condition. Fig. 5D(b–g) shows the experimental groups after 24 h of treatment, with decreased cell density, a significant deterioration in cell condition, and accompanying cell floating. Fig. 5D(i–m) shows the experimental groups after 48 h of treatment. Compared with the experimental group after 24 h of treatment, the cell density decreased further, and the number of floating dead cells increased significantly, showing dose- and time-dependence effects.

Hoechst 33258 is a cell-permeable benzimidazole dye that can bind to small grooves of double-stranded DNA and preferentially bind to sequences rich in adenine and thymine. When bound to DNA in living or fixed cells, it emits blue fluorescence (excitation at 352 nm/maximum emission wavelength at 461 nm) [37], which can be used as a nuclear marker for cell cycle research and to distinguish the nuclear morphology in apoptotic cells.

Fig. 5E(a) shows the control group. In this group, the nuclei of HepG2 cells appear uniformly pale blue with relatively smooth surfaces. Fig. 5E(b, c) shows the images after 24 h of treatment with CMCS-His-SA NPs. It was observed that, as concentration increased, cell density decreased, and chromatin became condensed and fragmented. Bright blue or even white fluorescence was observed under a fluorescence microscope.

The effect of CMCS-His-SA NPs on the migration of HepG2 cells

Bcl-2 and *Bax* are important regulators of mitochondrial apoptosis, with *Bcl-2* acting as an anti-apoptotic regulator and *Bax* being a pro-apoptotic regulator [35]. Fig. 6(A, B) shows that after 24 h of treatment with CMCS-His-SA NPs, the mRNA expression of anti-apoptotic regulator *Bcl-2* significantly decreased in a

concentration-dependent manner. The pro-apoptotic regulator *Bax* increased with increasing concentration of CMCS-His-SA NPs, and the mRNA expression of *Bcl-2*/*Bax* significantly decreased, indicating that CMCS-His-SA NPs can induce apoptosis in HepG2 cells.

The cell scratch assay is the main method used to evaluate cell migration ability [38]. As shown in Fig. 6(C), within 24 h of culture, the CMCS-His-SA nanoparticle-treated groups (200 and 400 μg/ml) exhibited significantly delayed migration compared with the negative control group (serum-free DMEM medium). The scratches in the control group gradually closed over time. In contrast, the scratch closure was delayed in the 200 and 400 μg/ml CMCS-His-SA nanoparticle-treated groups, with higher concentrations resulting in slower scratch closure. Statistical analysis showed that the scratch closure rate in the 400 μg/ml CMCS-His-SA nanoparticle-treated group was significantly lower than that in the control group at all points. These results indicate that CMCS-His-SA NPs significantly inhibit the migration of HepG2 cells in a dose-dependent manner.

Effect of CMCS-His-SA NPs on RAW264.7 macrophage activity

Cytotoxicity of CMCS and CMCS-His-SA blank nanoparticles toward macrophages

Fig. 6(D) shows the cytotoxicity of CMCS and CMCS-His-SA blank nanoparticles as determined using the CCK-8 assay kit. Within the concentration range of 25–800 μg/ml, the survival rate of RAW264.7 macrophages treated with CMCS and CMCS-His-SA blank nanoparticles remained above 90% after 24 h of treatment, indicating that both exhibited low cytotoxicity, with no significant difference between the two materials. To ensure that the selected concentrations were nontoxic, concentrations of 25–400 μg/ml were used in subsequent RAW264.7 macrophage activity assays.

Effects of CMCS and CMCS-His-SA NPs on macrophage proliferation

From Fig. 7(A, B), CMCS and CMCS-His-SA NPs can promote the proliferation of RAW264.7 macrophages, and the cell survival rate is significantly increased compared with the control group. At 24 h, a highly significant difference was observed between CMCS and CMCS-His-SA NPs at concentrations of 200–400 μg/ml. At 48 h, the proliferation effect gradually increased, and a highly significant difference was observed between CMCS and CMCS-His-SA NPs. Compared with CMCS, CMCS-His-SA NPs exhibited a time- and concentration-dependent proliferative effect on RAW264.7 macrophages. The highest proliferation effect of 400 μg/ml CMCS-His-SA NPs on RAW264.7 macrophages was 175.46%. The proliferative effect of CMCS on RAW264.7 macrophages at the same concentration was 143.9%. Previous studies have shown that anthocyanins from indigo fruit had a relatively small effect on the proliferation of RAW264.7 macrophages. Therefore, CMCS and CMCS-His-SA NPs were selected for subsequent immunological activity experiments.

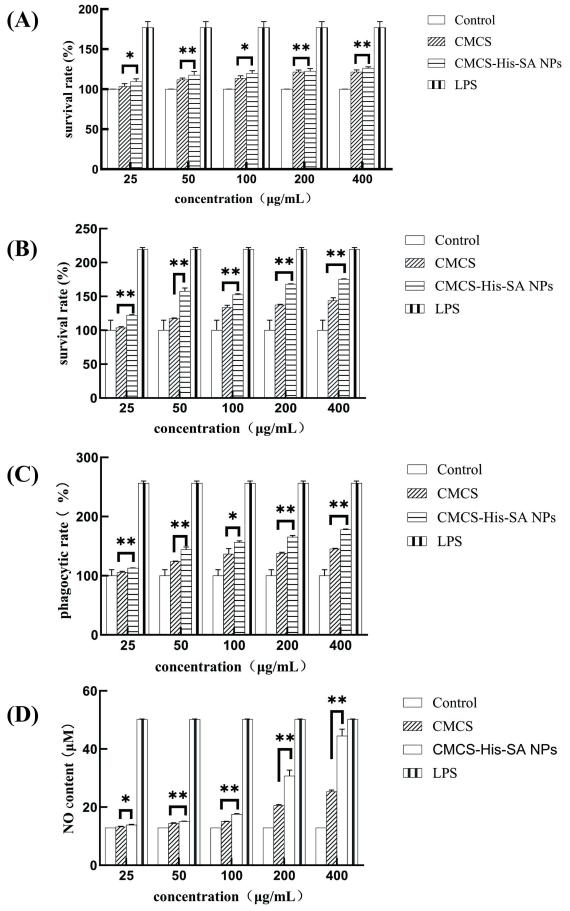

Fig. 7 (A, B) Effects of CMCS and NPs (NPs = CMCS-His-SA NPs) on the proliferation of RAW264.7 cells after 24 and 48 h of treatment; (C) The phagocytic ability of RAW264.7 cells; (D) NO secretion by RAW264.7 cells.

Effects of CMCS and CMCS-His-SA NPs on macrophage phagocytic ability

RAW264.7 macrophages play a crucial role in the body's immune defense by engulfing pathogenic microorganisms, secreting cytokines, hydrolyzing proteins, and presenting antigens [39, 40]. The effects of CMCS and CMCS-His-SA NPs on the phagocytic ability of RAW264.7 macrophages are shown in Fig. 7(C). The results indicate that both CMCS and CMCS-His-SA NPs can enhance the phagocytic ability of RAW264.7 macrophages. As the concentration increases, the difference in phagocytic ability between CMCS and CMCS-His-SA NPs gradually increases. At a concentration of 400 μg/ml, the phagocytic ability of

RAW264.7 macrophages treated with CMCS-His-SA NPs was 178.1%, which was 22% higher than that of CMCS. These results demonstrate that CMCS-His-SA NPs not only have cytotoxic effects on HepG2 cells but also exhibit strong immunological activity in RAW264.7 macrophages.

Effects of CMCS and CMCS-His-SA NPs on NO secretion by macrophages

NO is an inflammatory mediator that can be activated and secreted by RAW264.7 macrophages, which can inactivate ribonuclease and achieve the goal of clearing pathogens and tumor cells [40]. The results of the Griess assay for detecting the NO secretion of RAW264.7 macrophages are shown in Fig. 7(D). Compared with the control group, CMCS and CMCS-His-SA NPs can promote the NO secretion of RAW264.7 macrophages at 25 μg/ml, showing a significant difference. At concentrations of 50–400 μg/ml, CMCS and CMCS-His-SA NPs show highly significant differences in promoting NO secretion by RAW264.7 macrophages. The higher the concentration of CMCS and CMCS-His-SA NPs, the greater the NO secretion by RAW264.7 macrophages. At 400 μg/ml, CMCS-His-SA NPs promoted NO secretion to 47.03 μM.

CONCLUSION

In summary, results indicate that the successful coupling of CMCS-His-SA was demonstrated through proton NMR and infrared spectroscopy. The particle size of CMCS-His-SA blank nanoparticles at pH 7.4 is smaller than that under acidic conditions (pH 5.0). The critical micelle concentration of CMCS-His-SA blank nanoparticles is low, facilitating nanoparticle formation. In the characterization analysis of CMCS-His-SA NPs, the particle size at pH 7.4 is smaller than that under acidic conditions (pH 5.0). The zeta potential changes from negative at pH 7.4 to positive at pH 5.0, and the charge reverses. *In vitro* release studies showed that the drug release rate of CMCS-His-SA NPs was faster under acidic than under neutral conditions, demonstrating the successful preparation of pH-sensitive CMCS-His-SA NPs. As the concentration and treatment time of CMCS-His-SA NPs increase, the survival rate of HepG2 cells decreases. CMCS-His-SA NPs promote apoptosis of HepG2 cells by regulating the mRNA expression of pro-apoptotic regulator *Bax* and inhibiting the mRNA expression of anti-apoptotic regulator *Bcl-2*. The migration inhibitory effect of CMCS-His-SA NPs on HepG2 cells also increases with increasing concentration. Moreover, CMCS-His-SA NPs showed no cytotoxicity toward RAW264.7 macrophages at concentrations ranging from 25 to 800 μg/ml. In cell proliferation assays, with increasing drug concentration and treatment time, the proliferation rate of RAW264.7 macrophages increased, while their phagocytic and NO secretion abilities were also enhanced, thereby enhancing immunological activity.

Acknowledgements: This study was supported by the National Natural Science Foundation of China (No. 82303743) and Heilongjiang Province Outstanding Youth Project (No. YQ2024H030).

REFERENCES

1. Li J, Hoshino Y (2024) Elucidating the impact of ploidy level on biochemical content accumulation in haskap (*Lonicera caerulea* L. subsp. *edulis* (Turcz. ex Herder) Hultén) fruits: a comprehensive approach for fruit assessment. *Sci Hortic* **327**, 112831.
2. Cui J, Gao ZL, Li BS, Li JL, Li XY, Wang CY, Cheng DY, Dai CH (2020) Identification of anthocyanin biosynthesis related microRNAs and total microRNAs in *Lonicera edulis* by high-throughput sequencing. *J Genet* **99**, 31.
3. Li JX, Zhang XH, Lv JL, Yang J, Liu XC, Zhang XL, Zhang WT (2024) Fabrication and characterization of blue honeysuckle anthocyanins-loaded nanocomposite films and the application in pork preservation. *Food Hydrocolloids* **149**, 109600.
4. Wang YH, Gao NX, Nieto-Veloza A, Zhou LX, Sun XY, Si X, Tian JL, Lin Y, et al (2023) *Lonicera caerulea* polyphenols inhibit fat absorption by regulating Nrf2-ARE pathway mediated epithelial barrier dysfunction and special microbiota. *Food Sci Hum Wellness* **12**, 1309–1322.
5. Xue HK, Tan JQ, Cai X, Li Q, Tang JT (2021) Optimization ultrasound-assisted extraction of anthocyanins from cranberry using response surface methodology coupled with genetic algorithm and identification anthocyanins with HPLC-MS^2. *J Food Process Preserv* **45**, e15378.
6. Li WF, Zhang G, Tan S, Gong CQ, Yang YJ, Gu MY, Mi ZZ, Yang HY (2022) Polyacylated anthocyanins derived from red radishes protect vascular endothelial cells against palmitic acid-induced apoptosis via the p38 MAPK pathway. *Plant Foods Hum Nutr* **77**, 412–420.
7. Ali HM, Attia MH, Rashed EN (2024) Enhancing the stability of strawberry anthocyanins complexed to β-cyclodextrin and starch toward heat, oxidation, and irradiation. *ACS Omega* **9**, 5319–5329.
8. Chen YD, Fang CY, Huang JM, Pan H, He LP, Zhuang CL, Zheng XL (2024) The correlation between the main and minor lesions of synchronous multiple gastric neoplasms assessed gastroscopically and microscopically. *Surg Endosc* **38**, 1013–1019.
9. Liang LW, Luo RH, Huang ZL, Tang LN (2025) Clinical observation of nivolumab combined with cabozantinib in the treatment of advanced hepatocellular carcinoma. *World J Gastrointest Oncol* **17**, 103631.
10. Rostami M, Gharibshahian M, Mostafavi M, Sufali A, Golmohammadi M, Barati MR, Maleki R, Beheshtizadeh N (2025) A supervised machine-learning analysis of doxorubicin-loaded electrospun nanofibers and their anticancer activity capabilities. *Front Bioeng Biotechnol* **13**, 1493194.
11. Albin B, Adhikari P, Tiwari AP, Qubbaj K, Yang IH (2024) Electrical stimulation enhances mitochondrial trafficking as a neuroprotective mechanism against chemotherapy-induced peripheral neuropathy. *iScience* **27**, 109052.
12. Raut KK, Pandey S, Kharel G, Pascal SM (2024) Evidence of direct interaction between cisplatin and the caspase-cleaved prostate apoptosis response-4 tumor suppressor. *Protein Sci* **33**, e4867.

13. Fesenmeier DJ, Cooper ES, Won YY (2024) Overcoming limitations of conventional solvent exchange methods: achieving monodisperse non-equilibrium polymer micelles through equilibration-nanoprecipitation (ENP). *J Colloid Interface Sci* **661**, 861–869.
14. Fu ZL, Wang DS, Zheng CY, Xie MH, Chen YF, Zhou Y, Huang Y, Song Y, et al (2024) Elimination of intracellular Ca^{2+} overload by BAPTA-AM liposome nanoparticles: a promising treatment for acute pancreatitis. *Int J Mol Med* **53**, 34.
15. Li J, Wang F, Liu XY, Yang ZX, Hua XY, Zhu HQ, Valdivia CR, Xiao L, et al (2023) OpiCa1-PEG-PLGA nanomicelles antagonize acute heart failure induced by the cocktail of epinephrine and caffeine. *Mater Today Bio* **23**, 100859.
16. Xue H, Zha M, Tang Y, Zhao JD, Du XP, Wang Y (2024) Research progress on the extraction and purification of anthocyanins and their interactions with proteins. *Molecules* **29**, 2815.
17. Ionescu C, Samide A, Tigae C (2025) Trend in detection of anthocyanins from fresh fruits and the influence of some factors on their stability impacting human health: kinetic study assisted by UV-Vis spectrophotometry. *Antioxidants* **14**, 227.
18. Chandra Singh M, Price William E, Kelso C, Charlton K, Probst Y (2022) Impact of molar absorbance on anthocyanin content of the foods. *Food Chem* **386**, 132855.
19. Zhu JX, Guo XX, Guo TT, Yang Y, Cui XM, Pan J, Qu Y, Wang CX (2018) Novel pH-responsive and self-assembled nanoparticles based on *Bletilla striata* polysaccharide: preparation and characterization. *RSC Adv* **8**, 40308–40320.
20. Halah Talal S, Nawal AR (2025) Preparation and characterization of olmesartan medoxomil-loaded polymeric mixed micelle nanocarrier. *Iraqi J Pharm Sci* **33**, 89–100.
21. Aldawsari MF, Alam A, Imran M (2024) Rutin-loaded transethosomal gel for topical application: A comprehensive analysis of skin permeation and antimicrobial efficacy. *ACS Omega* **9**, 27300–27311.
22. Wang S, Lan Q, Badama S, Nashun BH, Wu Y, Bai YJ, Xu RH, Ta L, et al (2026) Impact of mare milk-derived small extracellular vesicles on proliferation, phagocytosis, and migration in RAW264.7 macrophage. *Sci Rep* **16**, 6944.
23. Zaheer Z, Alsubaie H, Kosa SA, Aazam ES (2024) Insights into the role of ionic surfactants on the morphology of gold and gold@silver nanoparticles. *J Mol Liq* **400**, 124565.
24. Jiang LQ, Zhang M, Bai YT, Cui FY, Zhang C, Wang ZY, Si SJ, Yang L, et al (2022) O-carboxymethyl chitosan based pH/hypoxia-responsive micelles relieve hypoxia and induce ROS in tumor microenvironment. *Carbohydr Polym* **275**, 118611.
25. Mubeen I, Abbas G, Shah SH, Assiri AA (2024) Conjugated linoleic acid-carboxymethyl chitosan polymeric micelles to improve the solubility and oral bioavailability of paclitaxel. *Pharmaceutics* **16**, 342.
26. Valderrama-Treviño AI, Castell-Rodríguez AE, Hernández-Muñoz R, Vázquez-Torres NA, Macari-Jorge A, Barrera-Mera B, Maciel-Cerda A, Vera-Graziano R, et al (2024) Development of a biodegradable prosthesis through tissue engineering, for the organ-replacement or substitution of the extrahepatic bile duct. *Ann Hepatol* **29**, 101530.
27. Wang L, Cai FQ, Li YX, Lin XL, Wang YT, Liang WJ, Liu CY, Wang CZ, et al (2024) pH-responsive block copolymer micelles of temsirolimus: preparation, characterization and antitumor activity evaluation. *Int J Nanomedicine* **19**, 9821–9841.
28. Zhang M, Ying N, Chen J, Wu LW, Liu HJ, Luo SH, Zeng DD (2024) Engineering a pH-responsive polymeric micelle co-loaded with paclitaxel and triptolide for breast cancer therapy. *Cell Proliferation* **57**, 13603.
29. Duong NT, Thiet TD, Anh TTP, Thi Lan P, Anh NgT, Lam TD (2024) Zerumbone delivery to tumor cells via pH-sensitive polymeric micelles. *Colloid Polym Sci* **302**, 237–251.
30. Fan Q, Zhang X, Zhang S, Cao ML, Zhang LY, Li L, Li WT, Zhang GM, et al (2025) Non-antibiotic nanoplatform based CuS/AuNCs@Lip NPs for inhibition pneumonia caused by MRSA and its mechanism exploration. *Mater Today Bio* **35**, 102603.
31. Zheng Y, Zhou Q, Ma H, Xu HL, Yin C, Su YH, Li YY, Li Y (2025) Revealing the incidence of the accelerated blood clearance phenomenon of PEGylated liposomes in individuals using a drug-release reporter liposoe. *Small* **21**, 2500526.
32. Qian Z, Li X, Yan G, Chen XY, Sajab MS, Ding GT, Wan J, Wan N (2025) Sodium alginate/carboxymethyl chitosan hydrogel microbeads for antibiotic adsorption in single and binary systems. *Gels* **11**, 646.
33. Kruczkowska W, Kłosiński KK, Grabowska KH, Gałęziewska J, Gromek P, Kciuk M, Kałuzińska-Kołat Ż, Kołat D, et al (2024) Medical applications and cellular mechanisms of action of carboxymethyl chitosan hydrogels. *Molecules* **29**, 4360.
34. Guyader N, Michiel M, Gauthier V, Serfaty S (2025) Critical micelle concentration determination with non-contact RF dielectric impedancemetry for surfactants in solution. *Colloids Surf A Physicochem Eng Asp* **725**, 137614.
35. Helmueller S, Lee S, Song XX, Kim DH, Lee YJ (2025) Tumoricidal efficacy of artesunate-eluting microsphere: differential role of Bax/Bak in orchestration of cell death pathways. *Biomater Res* **29**, 0217.
36. Witte I, Plappert U, de Wall H, Hartmann A (2007) Genetic toxicity assessment: employing the best science for human safety evaluation: part III: the comet assay as an alternative to in vitro clastogenicity tests for early drug candidate selection. *Toxicol Sci* **97**, 21–26.
37. Karg TJ, Golic KG (2018) Photoconversion of DAPI and hoechst dyes to green and red-emitting forms after exposure to UV excitation. *Chromosoma* **127**, 235–245.
38. Rossi M, Rossello S, Sallustio V, Mandrone M, Cerchiara T, Chiocchio I, Chidichimo G, Protti M, et al (2025) GinExtraMed: focus on *Rosa canina* L. extract encapsulated into glycethosomes and allanthosomes for accelerating skin wound healing. *Pharmaceutics* **17**, 5.
39. Kamali P, Fairn GD (2025) Using the sleeping beauty transposon system for doxycycline-inducible gene expression in RAW264.7 macrophage cells to study phagocytosis. *Bio Protoc* **15**, 3.
40. Moore TC, Pinkerton TS, Petro TM (2025) IRF3 promotes production of IL-6 and nitric oxide but represses CCL22 in RAW264.7 macrophage cells exposed to lipopolysaccharides in culture. *J Inflammation Res* **18**, 1255–1265.